The Modified Super-Ellipsoid yield criterion for human trabecular bone

Harun H. Bayraktar [1, 2,3]
Atul Gupta [1]
Ron Y. Kwon [1, 2]
Panayiotis Papadopoulos [2,3]
Tony M. Keaveny [1,2,4]

[1] Orthopaedic Biomechanics Laboratory, University of California, Berkeley, CA, USA
[2] Department of Mechanical Engineering, University of California, Berkeley, CA, USA
[3] Computational Solid Mechanics Laboratory, University of California, Berkeley, CA, USA
[4] Department of Bioengineering, University of California, Berkeley, CA, USA

Address for Correspondence and reprints:
Tony M. Keaveny, Ph.D.
6175 Etcheverry Hall
University of California
Berkeley, CA, 94720-1740, USA
+1-510-643-8017 (phone)
+1-510-642-6163 (fax)
tmk@me.berkeley.edu

Abstract

Despite the importance of multiaxial failure of trabecular bone in many biomechanics
applications, to date no complete multiaxial failure criterion for human trabecular bone has been
developed. By using experimentally validated nonlinear high-resolution, micro-mechanical finite
element models as a surrogate for multiaxial loading experiments, we determined the three-
dimensional normal strain yield surface and all combinations of the two-dimensional normal-
shear strain yield envelope. High-resolution finite element models of three human femoral neck
trabecular bone specimens obtained through micro-computed tomography were used. In total,
889 multiaxial-loading cases were analyzed, requiring over 41,000 CPU hours on parallel
supercomputers. Our results indicated that the multiaxial yield behavior of trabecular bone in
strain space was homogeneous across the specimens and nearly isotropic. Analysis of stress-
strain curves along each axis in the three-dimensional normal strain space indicated uncoupled
yield behavior, whereas substantial coupling was seen for normal-shear loading. A modified
super-ellipsoid surface with only four parameters fit the normal strain yield data very well with
an arithmetic error ± SD less than -0.04 ± 5.1%. Furthermore, the principal strains associated
with normal-shear loading showed excellent agreement with the yield surface obtained for
normal strain loading (arithmetic error ± SD < 2.5 ± 6.5%). We conclude that the four-parameter
"Modified Super-Ellipsoid" yield surface presented here describes the multiaxial failure behavior
of trabecular bone very well.

Introduction

Understanding the failure of trabecular bone under multiaxial loading is of great clinical importance. Trabecular bone within the proximal femur experiences multiaxial loads—which can lead to *in vivo* fracture of whole bones—during traumatic activities such as a fall [1, 2], and at bone-implant interfaces [3]. Formulation of a multiaxial failure criterion for trabecular bone can enable continuum-level finite element models of whole bones and bone-implant systems to mechanistically predict failure loads and failure sites under various loading scenarios. This in turn could improve hip fracture risk prediction with osteoporosis [4–6], assist in pre-surgical planning [7], and help better assess the effects of various drug treatments [8]. A multiaxial failure criterion is also of basic bioengineering interest since it represents a fundamental structure-function biomechanical characteristic of trabecular bone and as such may provide insight into biomimetic design of artificial materials.

Although the von Mises yield criterion has been used for trabecular bone [4], this theory does not account for the tension-compression strength asymmetry of trabecular bone [9, 10]. Cowin [11] proposed the quadratic Tsai-Wu [12, 13] failure criterion of the form:

$$f = f\left(\boldsymbol{\sigma}, \mathbf{H}, V_f\right) = 0, \tag{1}$$

in which $\boldsymbol{\sigma}$ is the stress tensor, $\mathbf{H}$ is the fabric tensor that characterizes the dependence of the Tsai-Wu coefficients on the structural anisotropy (i.e. architecture), and V_f is the volume fraction. Keaveny et al. [14] applied the Tsai-Wu theory to bovine tibial trabecular bone loaded by triaxial compressive stress and found only modest agreement with experimental data. Using a series of experimentally-validated nonlinear high-resolution finite element models as a surrogate for experiments, Niebur et al. [15] demonstrated that bovine trabecular bone under biaxial loading exhibits uncoupled failure envelopes in on-axis and transverse directions—similar to what has

been observed for certain cellular solid materials [16–19] and in the bovine triaxial normal stress experiments [14]. Within an anatomic site, it has been established that yield strains for trabecular bone under uniaxial [10], axial-shear [20] and biaxial loads [15] are independent of volume fraction, and that effects of architecture on uniaxial yield strains are minimal [21, 22]. Further, for combined tensile and shear loading, the maximum principal strain at yield was found to be very close to the uniaxial tensile yield strain [20], suggesting some form of a principal strain criterion may be a suitable candidate for trabecular bone under multiaxial loading.

The overall goal of this study was to determine a complete multiaxial yield envelope for human trabecular bone. Experimental data do not exist for this task, and all current data—experimental and computational—have been derived only for bovine trabecular bone. Human trabecular bone, however, differs from bovine bone in its architecture [22] and tissue material properties [23]. We focused here on human femoral neck trabecular bone due to its importance in hip fracture etiology. We used experimentally calibrated high-resolution, nonlinear finite element models [24] to circumvent difficulties involved in multiaxial mechanical testing and to eliminate the very large number of specimens required to address biological heterogeneity. Our specific objectives were to: 1) determine the three-dimensional normal strain yield surface, 2) determine the biaxial yield surface in all nine normal-shear planes, and 3) from these data, derive a robust multiaxial yield criterion that can be used in continuum-level finite element models. To the best of our knowledge, this is the first study to obtain a complete multiaxial yield criterion for any type of trabecular bone.

Methods

To overcome the difficulties in experimental investigation of the multiaxial strength of trabecular bone (e.g., load application, stress measurement, statistical power) we used experimentally validated high-resolution, micro-mechanical nonlinear finite element models. These specimen-specific models, obtained directly from high-resolution serial sectioning images [25] or micro-computed tomography [26], have shown excellent agreement with experimental data under uniaxial [27] and biaxial [15] loading conditions for bovine trabecular bone. Our overall strategy was to use these nonlinear models as a surrogate for experiments to obtain hundreds of multiaxial failure points for a single specimen, applying loading scenarios impossible to attain in a mechanical testing setting.

1. Specimens and finite element models

Micro-computed tomography (micro-CT-20, Scanco Medical AG, Bassersdorf, Switzerland) images—22 micron spatial resolution—of three human trabecular bone specimens from three cadavers (age-sex: 62-F, 63-M, and 72-M) were obtained (Fig. 1) and their architectural indices are given in Table 1. To save computational time, the micro-CT images were coarsened to obtain 5 mm cubic high-resolution finite element models with 66 micron hexahedral elements, using previously described protocols [24]. Numerical convergence studies have shown that this element size is sufficient for this type of trabecular bone [28]. Six linear elastic analyses were performed for each specimen to enforce alignment with the principal material orientations [29]. Images were rotated using the Euler angles of misalignment and this procedure was repeated until the deviation from orthotropic axes was less than 5 degrees. A bilinear principal strain-based asymmetric tissue material model was assumed for each element [24, 27]. Previously calibrated specimen-specific values of tissue elastic modulus were assigned

to each specimen and the same values of tissue yield strains in tension (0.41%) and compression (-0.83%) were assigned to all specimens [24].

2. *Obtaining the yield surface*

The yield surface in three-dimensional normal strain space was obtained by analyzing various load paths for each specimen (Fig. 2). Nonlinear finite element analysis was conducted using proportional loading and each load path was uniquely defined by the maximum strains applied in each direction. The three-dimensional normal strain space was spanned at two different angular increments (Fig. 2 left), of 15 degrees for two specimens and 22.5 degrees for one specimen, resulting in 266 and 114 load paths, respectively. For each load path, stress-strain curves were obtained and 0.2% offset yield strains were calculated. The first chronological yield point—in loading history—was used to construct the yield surface (Fig. 3).

The yield envelopes in all nine normal-shear strain planes (i.e. ε_{xx}-γ_{xy}, ε_{xx}-γ_{yz}, ε_{xx}-γ_{xz} etc.) were also obtained for all three specimens (Fig. 2 right). In each of these planes, nine load paths were considered with 18 degrees increments totaling 81 analyses. Altogether, 889 analyses were performed on IBM SP2 and SP3 parallel supercomputers that required a total of approximately 41,500 hours CPU time.

3. *Mathematical modeling*

Once the yield envelope data were determined, we sought to find an explicit mathematical representation that could subsequently be used in continuum level finite element models. Motivated by evidence that a principal strain type criterion may be successful [20], we formulated a "modified super-ellipsoid" (MSE) yield surface in three-dimensional principal strain space as follows:

$$g(\varepsilon_1,\varepsilon_2,\varepsilon_3) = \left[\left| \frac{\varepsilon_1 - c_1}{r_1} \right|^{2/n_2} + \left| \frac{\varepsilon_2 - c_2}{r_2} \right|^{2/n_2} \right]^{n_2/n_1} + \left| \frac{\varepsilon_3 - c_3}{r_3} \right|^{2/n_1} + \left| \frac{t(\varepsilon_1 + \varepsilon_2 + \varepsilon_3)}{r_1 + r_2 + r_3} \right|^{2/n_1} - 1, \qquad (2)$$

in which, ε_i (i=1, 2, 3) are the principal strains, r_i (i=1, 2, 3) are the radii, c_i (i=1, 2, 3) are the

shift in the center coordinates with respect to the origin, n_1 and n_2 are "squareness" parameters,

and t is a "flattening" parameter. The shape of this yield surface is a modification of a standard

super-ellipsoid [30] by inclusion of the third term, which sharpens the purely tensile octant and

flattens the compressive octant. In the case when $r_1 = r_2 = r_3$, $c_1 = c_2 = c_3$, and the squareness

parameters are the same $n_1 = n_2$, the yield surface is identical in three biaxial principal strain

planes. With these simplifications, a four-parameter (r, c, n, and t), isotropic version of the yield

surface was determined:

$$g(\varepsilon_1,\varepsilon_2,\varepsilon_3) = \sum_{i=1}^{3} \left| \frac{\varepsilon_i - c}{r} \right|^{2/n} + \left| t \frac{\mathrm{tr}(\boldsymbol{\varepsilon})}{3r} \right|^{2/n} - 1. \qquad (3)$$

The error norm in the approximation of any yield point using the yield functions (2) and

(3) was compared to the envelope determined by the finite element analyses and was defined

using the standard vector norm as:

$$\text{Error norm } (\%) = \frac{\left\| \boldsymbol{\varepsilon}_{\text{surface}} - \boldsymbol{\varepsilon}_{\text{FEA}} \right\|}{\left\| \boldsymbol{\varepsilon}_{\text{FEA}} \right\|} \times 100, \qquad (4)$$

in which $\boldsymbol{\varepsilon}_{\text{surface}}$ is the vector of the closest point on the yield surface to the yield point $\boldsymbol{\varepsilon}_{\text{FEA}}$,

determined by nonlinear finite element analyses. The nine parameters in (2) and four parameters

in (3) were determined by using a standard nonlinear optimization algorithm in Matlab (v6.5,

The Mathworks, Natick, MA) to minimize the mean error norm for 646 yield points in the three-

dimensional normal strain space for all three specimens.

4. Testing the yield surface

To evaluate the success of the proposed principal strain yield functions in predicting yielding for more general loading modes, we used the normal-shear yield points to calculate principal yield strains for each loading path and specimen. For this case, the principal strain directions did not coincide with the principal material orientation and hence provided a means to check if multiaxial yield is indeed associated with principal strains, and, if it is isotropic. The principal yield strains ($\boldsymbol{\varepsilon}_{\text{principal}}$) obtained from the normal-shear load cases were then compared against the yield surface given by the calibrated form of (3) and a prediction error was quantified as:

$$\text{Prediction Error } (\%) = \frac{\left\| \boldsymbol{\varepsilon}_{\text{Eqn.3}} - \boldsymbol{\varepsilon}_{\text{principal}} \right\|}{\left\| \boldsymbol{\varepsilon}_{\text{principal}} \right\|} \times 100. \tag{5}$$

Results

The yield behavior under multiaxial loading was homogeneous and nearly isotropic. Yield points in strain-space were remarkably similar not only for all three specimens but also for all three biaxial planes (Fig. 4). Quadratic fits to the data indicated that failure along each axis was largely independent (Fig. 4), although there was some interaction. The largest interaction was observed under triaxial compression—analogous to hydrostatic stress—for which the yield strain was as much as 39% lower than the uniaxial compressive strain. This effect can also be seen in the purely compressive quadrant in all biaxial planes (Fig. 4).

Normal-shear yield behavior strongly depended on the particular normal and shear combination (Fig. 5), indicating anisotropy in this aspect of the failure behavior. For the combination of axial loads and transverse shear (e.g., ε_{xx}-γ_{yz}, ε_{yy}-γ_{xz}, ε_{zz}-γ_{xy}), the yield strain along

the shear axis showed little coupling. When the normal strain was in the same plane as the shear strain (e.g., ε_{xx}-γ_{xy}, ε_{xx}-γ_{xz}, ε_{yy}-γ_{xy}, ε_{yy}-γ_{yz}, ε_{zz}-γ_{yz}, ε_{zz}-γ_{xz}), the normal-shear interaction was more substantial. This can be observed as the greater reduction in shear yield strain when normal strain is applied simultaneously.

The MSE yield surface with nine independent coefficients (Table 2) was calibrated to fit the three-dimensional normal strain-space yield data with a mean ± SD error norm of 3.7 ± 3.1% (Max. 15.6%) and arithmetic error of -0.06 ± 4.8% (Fig. 6). For the four parameter criterion, the error norm was only 3.9 ± 3.3% (Max. 17.3%) with an arithmetic error of -0.04 ± 5.1% (Table 2, Fig. 4, and Fig. 6–7), resulting in the following equation, in which ε is given in %:

$$g(\varepsilon_1, \varepsilon_2, \varepsilon_3) = 4.33 \sum_{i=1}^{3} (\varepsilon_i + 0.16)^{4.83} + 0.12 \cdot (\mathrm{tr}\,\boldsymbol{\varepsilon})^{4.83} - 1. \tag{6}$$

Finally, the yield surface (6) was highly successful in predicting yielding for the normal-shear loading for which it was not calibrated. In this instance, the prediction error norm (mean ± SD) combined for all three specimens (243 load cases) was 5.5 ± 4.2% (Max. 18.2%) with a mean arithmetic error of 2.5 ± 6.5%.

Discussion

The overall goal of this study was to investigate the multiaxial yield behavior of human femoral neck trabecular bone and from that obtain a multiaxial yield criterion. Our results show that in strain space the yield behavior under multiaxial loading was nearly homogeneous and isotropic. Independent analysis of stress-strain curves to obtain yield points along each loading axis indicated negligible coupling in normal strain yield behavior, but sometimes appreciable coupling for normal-shear behavior. This overall behavior was described very well by our

"modified super-ellipsoid" (MSE) criterion, using only four parameters. Further, the MSE criterion was formulated in terms of principal values and trace of the strain tensor, and the normal-shear yield data, when transformed into principal strain space, agreed well with this formulation. Taken together, these results indicate that the multiaxial yield behavior of the femoral neck trabecular bone studied here shows isotropic and homogeneous behavior in principal strain-space and this behavior can be successfully represented by a continuous and smooth four-parameter mathematical function, termed here the Modified Super-Ellipsoid (MSE) yield criterion.

Several aspects of this study support the validity of our results. The finite element models used were non-linear with material properties that were calibrated from specimen-specific mechanical testing data [24]. These models provided a number of advantages. First, data points for the yield surface were obtained by testing along hundreds of load paths for each specimen, which is impossible to do with real experiments due to the destructive nature of each mechanical test. In addition, the biological heterogeneity of human bone samples would necessitate a very large sample size to conduct a comparable study. Second, application of multiaxial loading boundary conditions and measurement of strains was relatively easy in comparison to the challenges present in an experimental approach [14, 20]. Third, the yield surface was formulated in strain space, which eliminated the strong dependency of the formulated criterion on the apparent density of each specimen. Finally the proposed yield function (6) for human femoral trabecular bone has only four coefficients in its reduced form and is a smooth and continuous function of the strain tensor. These properties facilitate implementation of this yield function in the material constitution of continuum-level finite element models for prediction of failure of whole bones.

Despite these strengths, certain caveats exist. Only three specimens were analyzed from a single site. The range of volume fraction, 0.28–0.38, spanned by these specimens may limit the applicability of the yield surface obtained here to trabecular bone from other anatomic sites such as the greater trochanter, proximal tibia or the human vertebra, all having much lower density and different architecture. Geometrical nonlinearities (e.g. bending, buckling) are expected to play an important role in the mechanical behavior of trabecular bone from these latter sites due to the lower density and variations that may exist in architectural properties (see Appendix) [22, 31–33]. Interestingly the normal-shear yield behavior determined in this study is remarkably similar to previously reported experimental data on bovine trabecular bone [20], suggesting that for high-density trabecular bone at least, architecture is not critical. With the addition of geometrical nonlinearities to the finite element formulation and use of site-specific tissue material properties, it should be possible to extend the methods of the present study to obtain a multiaxial yield criterion for other human anatomic sites and as a function of age, disease, and drug treatment.

Our multiaxial yield data for human bone complement previous experimental [14, 20, 34] and computational [15] studies on multiaxial failure of bovine trabecular bone. The stress-based quadratic Tsai-Wu criterion has been the main focus of studies investigating a suitable failure criterion for trabecular bone since this theory incorporates the asymmetry and anisotropy of trabecular bone strength [11, 14]. However, after calibration using experimental data, the Tsai-Wu criterion was not successful in predicting yielding for triaxial compressive loading [14]. The experimental data obtained in these triaxial experiments indicated uncoupling of yielding along each loading axis and the discrepancy is due to the fact that the Tsai-Wu criterion imposes excessive interaction between loading modes [14]. In support of this argument, less interaction

has been observed in the present study and in a study on bovine trabecular bone [15], which results in the uncoupling of the yield curves along each loading axis. This uncoupling in multiaxial normal loading has also been reported for cellular solid type materials [16–19]. Furthermore, investigation of the distribution of yielded tissue in trabecular bone under biaxial loading has shown that the locations of the damaged material depend on the apparent level loading direction [15].

While most behavior observed in multiaxial normal loading was isotropic, the yield behavior for different combinations of normal-shear loading showed different levels of interactions between the loading modes (Fig. 5) and displayed transversely isotropic behavior. When the trabecular bone was loaded such that the normal strain was in the plane of shear (e.g., ε_x-γ_{xy}, ε_x-γ_{xz}, ε_y-γ_{xy}, ε_y-γ_{yz}, ε_z-γ_{yz}, ε_z-γ_{xz}), there was a high level of interaction which is reflected in the "curviness" of the fits in Fig. 5. However, for the case when shear was applied out-of-plane (e.g., ε_x-γ_{yz}, ε_y-γ_{xz}, ε_z-γ_{xy}), the interaction was less coupled, resulting in almost flat curves along each loading direction, similar to the behavior under biaxial normal strain (Fig. 4). This interaction between normal and shear strains has been demonstrated theoretically [20]. This is a result of the architecture of trabecular bone, modeled simply as parallel columns in a cellular solid model [20]. In this model and for loading in the principal material co-ordinate system, when the normal load is applied in the plane of shear (e.g., ε_x-γ_{xy}, ε_x-γ_{xz}, ε_y-γ_{xy}, ε_y-γ_{yz}, ε_z-γ_{yz}, ε_z-γ_{xz}), aligned trabeculae in the normal loading direction support both normal and shear loads and the direct load-carrying role of transverse trabeculae is minimal (this may not hold in very low density bone, in which the transverse trabeculae may provide important lateral stability to the vertical trabeculae). However, when the normal load is perpendicular to the plane of shear (e.g., ε_x-γ_{yz}, ε_y-γ_{xz}, ε_z-γ_{xy}), transverse trabeculae are loaded by the shear load while the normal load is

supported by the longitudinal trabeculae. In this way, there is coupling for in-plane loading and uncoupling for out-of-plane normal-shear loading.

Although the modified super-ellipsoid (MSE) yield surface was calibrated based on yield data obtained in the principal material coordinate system and under normal strains, it performed exceptionally well in predicting yielding for normal-shear loading. The reasons for this are twofold. First, trabecular bone exhibits nearly isotropic uniaxial yield behavior in normal strain-space [35, 36]. Because of this, and because the multiaxial normal strain behavior is mostly uncoupled, the transverse isotropy in yield behavior in the normal-shear planes (Fig. 5) is transformed into isotropic failure in principal strain space. When the shear is out of plane, the applied normal strain remains as a principal strain and the out-of-plane shear transforms into principal strains in the other two orthogonal directions. For the case when shear and normal strains are in the same plane, the resulting two principal strains (the third is equal to zero) remain in the plane and one becomes greater in magnitude than the other due to the superposition of the strains. It also happens that, shear yield strains of trabecular bone, when rotated into principal strain space, fall close to the surface obtained in three-dimensional normal strain space and are about twice the value of the uniaxial tensile yield strain [20]. A mechanistic explanation of this is that shear loading causes bending of trabeculae, which then fail at the hard tissue level because of high tensile strains.

The simple nature of the four-parameter MSE yield criterion is clinically significant for two reasons. First, it can be implemented into continuum level finite element analyses used to improve failure predictions of whole bone and bone-implant systems. The function is convex and smooth with continuous derivatives ($\partial g/\partial \boldsymbol{\varepsilon}$, $\partial^2 g/\partial \boldsymbol{\varepsilon}\partial \boldsymbol{\varepsilon}$), which is a desirable numerical trait in the implementation of plasticity algorithms [37]. Second, only four experiments are necessary to

calibrate the four independent parameters: r, c, n, and t of the MSE yield criterion. We suggest using uniaxial tensile and compressive strain tests to determine c and r, since for these loading cases the other parameters have a negligible effect in determining the yield function. To determine t, a triaxial compression or tension load case is required. A biaxial yield point is required for n, which controls the curvature of the surface at the corners. While all these tests are difficult to perform in the laboratory, high-resolution finite element analysis can be used to obtain the necessary data. If successful, this approach would greatly facilitate the investigation of the effects of aging, disease, and drug treatments on this important aspect of trabecular bone strength behavior.

Appendix

To justify our use of the small deformation assumption in our finite element analyses, we investigated the effects of geometrical nonlinearities on the elastic tensile, compressive, and shear behaviors of trabecular bone from human femoral neck (V_f=28.9%), proximal tibia (V_f =11.0%), greater trochanter (V_f=9.5%), and vertebral body (V_f=8.0%). The trabecular tissue was modeled as a Neo-Hookean (elastic) material with 1 GPa tissue modulus and a Poisson's ratio of 0.3. Three uniaxial boundary conditions were applied for each specimen: tension, compression, and shear. All geometrically nonlinear analysis results were compared against those obtained using the small deformation assumption. Analyses were performed using a custom parallel finite element code [38] on an IBM SP3 parallel supercomputer.

The stress-strain curves exhibited the same trends for all anatomic sites. Nonlinear tensile loading caused stiffening, while nonlinear compression and shear resulted in softening (Fig. 8). With increasing volume fraction, the effect of geometrically nonlinear deformations—quantified here as the difference in stresses at 0.5% apparent strain—decreased and was minimal for the femoral neck trabecular bone. Shear loading was observed to have the least differences in stresses between linear and nonlinear models.

These results indicate that geometrically nonlinear deformations do play a role in the mechanical behavior of low-density trabecular bone, even at relatively small strains, but that for high-density ($\rho > 0.4$ g/cc or $V_f > 20\%$) trabecular bone from the femoral neck, the small deformations assumption is reasonable.

References

[1]   Lotz, J. C., Cheal, E. J., and Hayes, W. C., 1991, "Fracture prediction for the proximal femur using finite element models: Part I-Linear analysis," J. Biomech. Eng. **113**, pp. 353-360.

[2]   Lotz, J. C., Cheal, E. J., and Hayes, W. C., 1991, "Fracture prediction for the proximal femur using finite element models: Part II--Nonlinear analysis," J. Biomech. Eng. **113**, pp. 361-365.

[3]   Cheal, E. J., Hayes, W. C., Lee, C. H., Snyder, B. D., and Miller, J., 1985, "Stress analysis of a condylar knee tibial component: influence of metaphyseal shell properties and cement injection depth," J. Orthop. Res. **3**, pp. 424-434.

[4]   Keyak, J. H., and Rossi, S. A., 2000, "Prediction of femoral fracture load using finite element models: an examination of stress- and strain-based failure theories," J. Biomech. **33**, pp. 209-214.

[5]   Cody, D. D., Gross, G. J., Hou, F. J., Spencer, H. J., Goldstein, S. A., and Fyhrie, D. P., 1999, "Femoral strength is better predicted by finite element models than QCT and DXA," J. Biomech. **32**, pp. 1013-1020.

[6]   Ford, C. M., Keaveny, T. M., and Hayes, W. C., 1996, "The effect of impact direction on the structural capacity of the proximal femur during falls," J. Bone Miner. Res. **11**, pp. 377-383.

[7]   Liebschner, M. A. K., Rosenberg, W. S., and Keaveny, T. M., 2001, "Effects of bone cement volume and distribution on vertebral stiffness after vertebroplasty," Spine **26**, pp. 1547-1554.

[8] Oden, Z. M., Selvitelli, D. M., and Bouxsein, M. L., 1999, "Effect of local density changes on the failure load of the proximal femur," J. Orthop. Res. **17**, pp. 661-667.

[9] Keaveny, T. M., Wachtel, E. F., Ford, C. M., and Hayes, W. C., 1994, "Differences between the tensile and compressive strengths of bovine tibial trabecular bone depend on modulus," J. Biomech. **27**, pp. 1137-1146.

[10] Morgan, E. F., and Keaveny, T. M., 2001, "Dependence of yield strain of human trabecular bone on anatomic site," J. Biomech. **34**, pp. 569-577.

[11] Cowin, S. C., 1986, "Fabric dependence of an anisotropic strength criterion," Mech. Mater. **5**, pp. 251-260.

[12] Tsai, S., and Wu, E., 1971, "A general theory for strength of anisotropic materials," J. Comp. Mat. **5**, pp. 58-80.

[13] Wu, E., 1974, "Phenomenological anisotropic failure criterion.," *Mechanics of Composite Materials*, G. Sendecky, ed., Academic Press, New York, pp. 353-431.

[14] Keaveny, T. M., Wachtel, E. F., Zadesky, S. P., and Arramon, Y. P., 1999, "Application of the Tsai-Wu quadratic multiaxial failure criterion to bovine trabecular bone," J. Biomech. Eng. **121**, pp. 99-107.

[15] Niebur, G. L., Feldstein, M. J., and Keaveny, T. M., 2002, "Biaxial failure behavior of bovine tibial trabecular bone," J. Biomech. Eng. **124**, pp. 699-705.

[16] Patel, M. R., 1969, "The deformation and fracture of rigid cellular plastics under multiaxial stress," p. 196. Berkeley, CA: University of California, Berkeley, CA.

[17] Zaslawsky, M., 1973, "Multiaxial-stress studies on rigid polyurethane foam," Exper Mech **2**, pp. 70-76.

[18]   Gibson, L. J., Ashby, M. F., Zhang, J., and Triantafillou, T. C., 1989, "Failure surfaces for cellular materials under multiaxial loads-I. Modelling," Int. J. Mech. Sci. **31**, pp. 635-663.

[19]   Triantafillou, T. C., Zhang, J., Shercliff, T. L., Gibson, L. J., and Ashby, M. F., 1989, "Failure surfaces for cellular materials under multiaxial loads-II. Comparison of models with experiment," Int. J. Mech. Sci. **31**, pp. 665-678.

[20]   Fenech, C. M., and Keaveny, T. M., 1999, "A cellular solid criterion for predicting the axial-shear failure properties of trabecular bone.," J. Biomech. Eng. **121**, pp. 414-422.

[21]   Bayraktar, H. H., and Keaveny, T. M., 2003, "Mechanisms of uniformity of yield strains for trabecular bone," J. Biomech. **In Review**.

[22]   Morgan, E. F., Bayraktar, H. H., Yeh, O. C., and Keaveny, T. M., 2003, "Contribution of inter-site variations in architecture to trabecular bone apparent yield strain," J. Biomech. **In Review**.

[23]   Guo, X. E., 2001, "Mechanical properties of cortical bone and cancellous tissue," *Bone Mechanics Handbook*, S. C. Cowin, ed., CRC Press, Boca Raton, pp. 10.11-10.23.

[24]   Bayraktar, H. H., Morgan, E. F., Niebur, G. L., Morris, G., Wong, E. K., and Keaveny, T. M., 2003, "Comparison of the elastic and yield properties of human femoral trabecular and cortical bone tissue," J. Biomech. **In Press**.

[25]   Beck, J. D., Canfield, B. L., Haddock, S. M., Chen, T. J. H., Kothari, M., and Keaveny, T. M., 1997, "Three-dimensional imaging of trabecular bone using the computer numerically controlled milling technique," Bone **21**, pp. 281-287.

[26]   Rüegsegger, P., Koller, B., and Müller, R., 1996, "A microtomographic system for the nondestructive evaluation of bone architecture," Calcif. Tissue Int. **58**, pp. 24-29.

[27]   Niebur, G. L., Feldstein, M. J., Yuen, J. C., Chen, T. J., and Keaveny, T. M., 2000, "High-resolution finite element models with tissue strength asymmetry accurately predict failure of trabecular bone," J. Biomech. **33**, pp. 1575-1583.

[28]   Niebur, G. L., Yuen, J. C., Hsia, A. C., and Keaveny, T. M., 1999, "Convergence behavior of high-resolution finite element models of trabecular bone," J. Biomech. Eng. **121**, pp. 629-635.

[29]   Van Rietbergen, B., Odgaard, A., Kabel, J., and Huiskes, R., 1996, "Direct mechanics assessment of elastic symmetries and properties of trabecular bone architecture," J. Biomech. **29**, pp. 1653-1657.

[30]   Barr, A. H., 1981, "Superquadratics and angle-preserving transformations," IEEE Computer Graphics and Applications **1**, pp. 11-23.

[31]   Hildebrand, T., Laib, A., Müller, R., Dequeker, J., and Rüegsegger, P., 1999, "Direct three-dimensional morphometric analysis of human cancellous bone: microstructural data from spine, femur, iliac crest, and calcaneus," J. Bone Miner. Res. **14**, pp. 1167-1174.

[32]   Müller, R., Gerber, S. C., and Hayes, W. C., 1998, "Micro-compression: a novel technique for the nondestructive assessment of local bone failure," Technol. Health Care **6**, pp. 433-444.

[33]   Stolken, J. S., and Kinney, J. H., 2003, "On the importance of geometric nonlinearity in finite-element simulations of trabecular bone failure," Bone **33**, pp. 494-504.

[34]   Stone, J. L., Beaupre, G. S., and Hayes, W. C., 1983, "Multiaxial strength characteristics of trabecular bone," J. Biomech. **16**, pp. 743-752.

[35]   Turner, C. H., 1989, "Yield behavior of bovine cancellous bone," J. Biomech. Eng. **111**, pp. 256-260.

[36] Chang, W. C. W., Christensen, T. M., Pinilla, T. P., and Keaveny, T. M., 1999, "Isotropy of uniaxial yield strains for bovine trabecular bone," J. Orthop. Res. **17**, pp. 582-585.

[37] Simo, J. C., and Hughes, T. J. R., 1998, "Computational Inelasticity," Springer-Verlag, New York.

[38] Adams, M., 2002, "Evaluation of three unstructured multigrid methods on 3D finite element problems in solid mechanics," Int. J. Num. Meth. Eng. **55**, pp. 519-534.

Table 1: Characteristics of each specimen and number of finite element analyses performed.

Sex	Age	V_f	Tb.Th mean ± S.D.	Tb.Sp mean ± S.D.	DA	SMI	3D normal strain analyses	normal-shear analyses
F	62	0.28	0.18 ± 0.06	0.58 ± 0.20	1.91	-0.13	144	81
M	63	0.29	0.19 ± 0.07	0.64 ± 0.20	1.63	0.11	266	81
M	72	0.38	0.25 ± 0.09	0.63 ± 0.20	1.86	-0.82	266	81
						Total	*646*	*243*

KEY: V_f: volume fraction (BV/TV); Tb.Th, mean trabecular thickness (mm); Tb.Sp, mean trabecular spacing (mm); DA, degree of anisotropy; SMI, structural model index. S.D. for the Tb.Th. and Tb.Sp. parameters indicates intraspecimen variations. All measurements were made using the TRI method [31].

Table 2: Coefficients of the modified super-ellipsoid yield surface given in Eq. (2) and (3). The radius and center has units of % strain; n and t are dimensionless.

Full Coefficient List		Reduced Coefficient List*	
r_1	0.728	r	0.738
r_2	0.719	c	-0.157
r_3	0.753	n	0.414
c_1	-0.145	t	1.417
c_2	-0.152		
c_3	-0.169		
n_1	0.426		
n_2	0.347		
t	1.396		

* $r_1 = r_2 = r_3$, $c_1 = c_2 = c_3$, and $n_1 = n_2$ assumed

Figure Captions

Figure 1: Renderings of the three five-millimeter cube trabecular bone specimens used to develop the multiaxial yield criterion. Age, sex, and volume fraction (V_f) information is shown. See Table 1 for architectural indices.

Figure 2: Illustration of the method by which the load paths were determined in three-dimensional normal strain space (left) and in normal-shear strain planes (right). For the three-dimensional normal strain case, after a plane was spanned at an angular increment of θ, the plane itself was rotated about the x-axis by the same angle. A similar approach was taken for the nine normal-shear planes. Note that only one of the nine normal-shear strain combinations is shown.

Figure 3: Apparent level stress vs. normalized strain plot for a sample load path in three-dimensional normal strain space. The 0.2%-offset lines (thin dash) used to determine yield strains along each loading axis are also shown. The normalized strain (the strain along each direction divided by the maximum strain applied in that direction) was used to illustrate chronological yielding in all three directions (marked as points a, b, and c). In this case, yielding first occurred along the x-axis (a), then along the y-axis (b), and finally along the z-axis (c). At the first chronological yield point (a) the strains in the other two directions were calculated to obtain the failure point for the three-dimensional yield surface.

Figure 4: Yield envelopes in three biaxial normal strain planes: (a) ε_{xx}-ε_{yy}, (b) ε_{yy}-ε_{zz}, (c) ε_{xx}-ε_{zz}. Circles indicate the yield data from all three specimens; solid symbols indicate yielding along the vertical axis; empty symbols indicate yielding along the horizontal axis. Dashed lines shown are

quadratic fits to the yield points along each axis. The closed inscribed envelope shown in (a), (b), and (c) is the proposed yield surface (four-parameter modified super-ellipsoid) cross-section in each biaxial normal strain plane.

Figure 5: Yield envelopes in the nine normal-shear planes: (a) ε_{xx}-γ_{xy}, (b) ε_{xx}-γ_{yz}, (c) ε_{xx}-γ_{xz}, (d) ε_{yy}-γ_{xy}, (e) ε_{yy}-γ_{yz}, (f) ε_{yy}-γ_{xz}, (g) ε_{zz}-γ_{xy}, (h) ε_{zz}-γ_{yz}, (i) ε_{zz}-γ_{xz}. Square, triangle, and circle indicate the three different specimens. Solid symbols indicate yielding along the shear axis while empty symbols indicate yielding along the normal loading direction. Dashed lines shown are quadratic fits to the yield points along each axis. Solid lines are fourth order polynomial fits to the yield points along the shear axis.

Figure 6: Histogram of percentage arithmetic error of the yield surface representation for the full (9 coefficients) and reduced (4 coefficients) modified super-ellipsoids vs. the finite element data.

Figure 7: Yield surface (266 points) plotted in three-dimensional normal strain space for one of the specimens (63-M) (left). The four-parameter modified super-ellipsoid yield surface given by Eq. (6) is shown on the right for comparison.

Figure 8: Differences in stresses between nonlinear vs. linear solutions ($\Delta\sigma/\sigma_{\text{linear}}$) at 0.5% strain decreased with increasing volume fraction. Inclusion of geometrically nonlinear deformations had the least effect in shear loading. For compression and shear, a softening effect was observed, but is shown here using positive values of percentage difference. A stiffening effect was seen in tension.
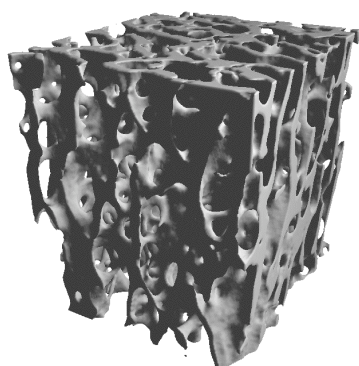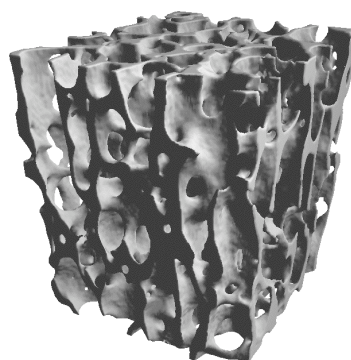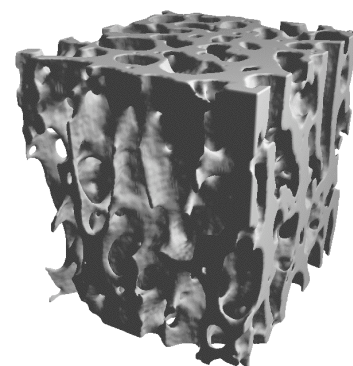
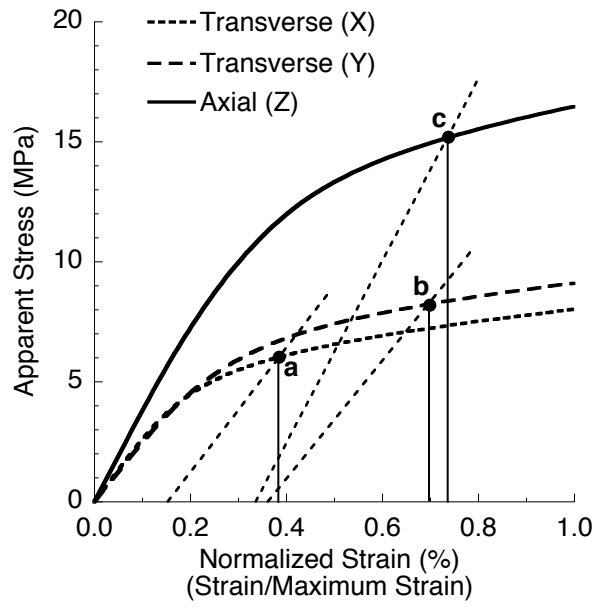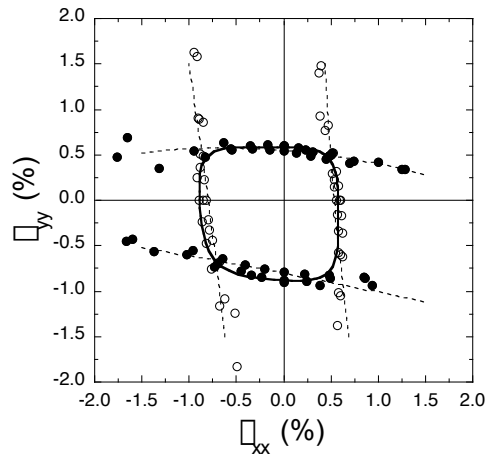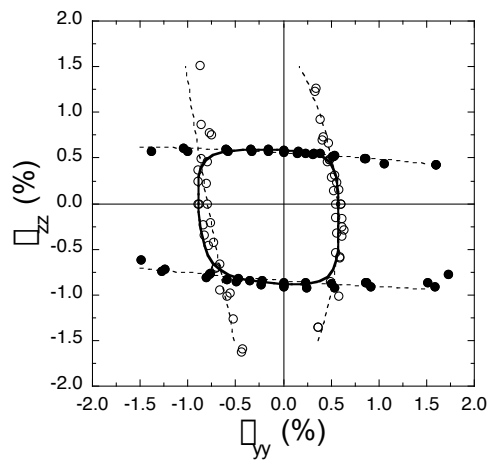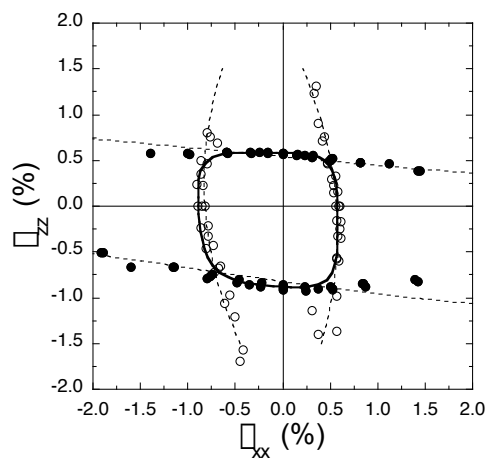| 62-F	63-M	72-M
$V_f = 28\%$	$V_f = 29\%$	$V_f = 38\%$
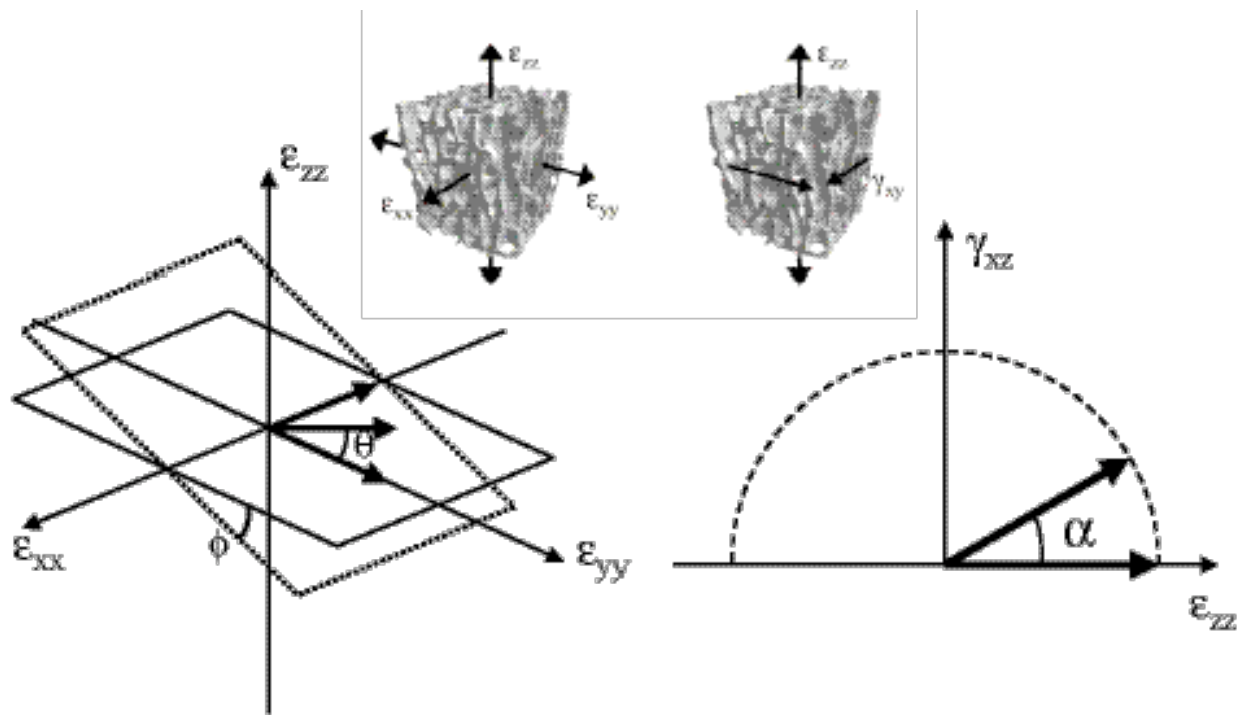
Figure 1
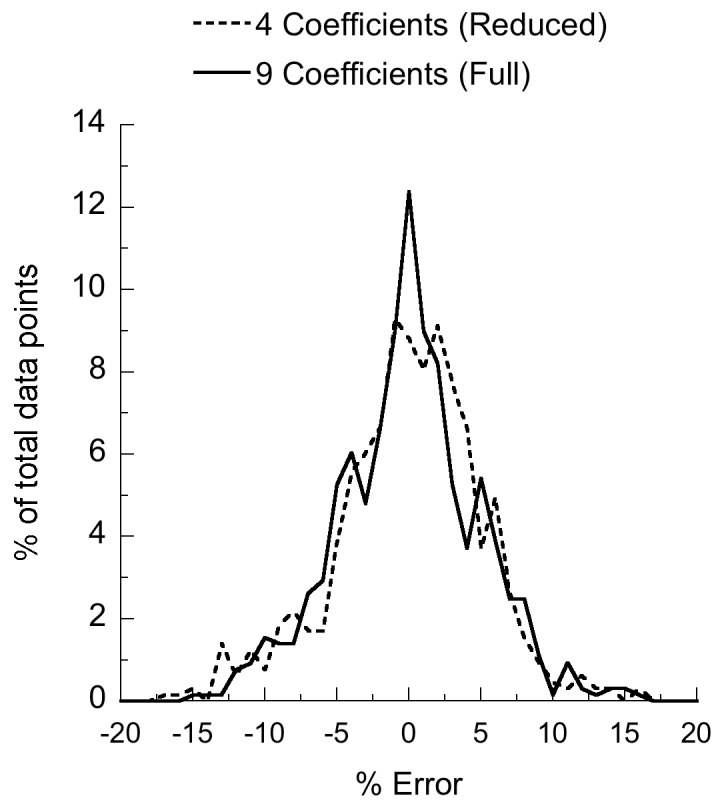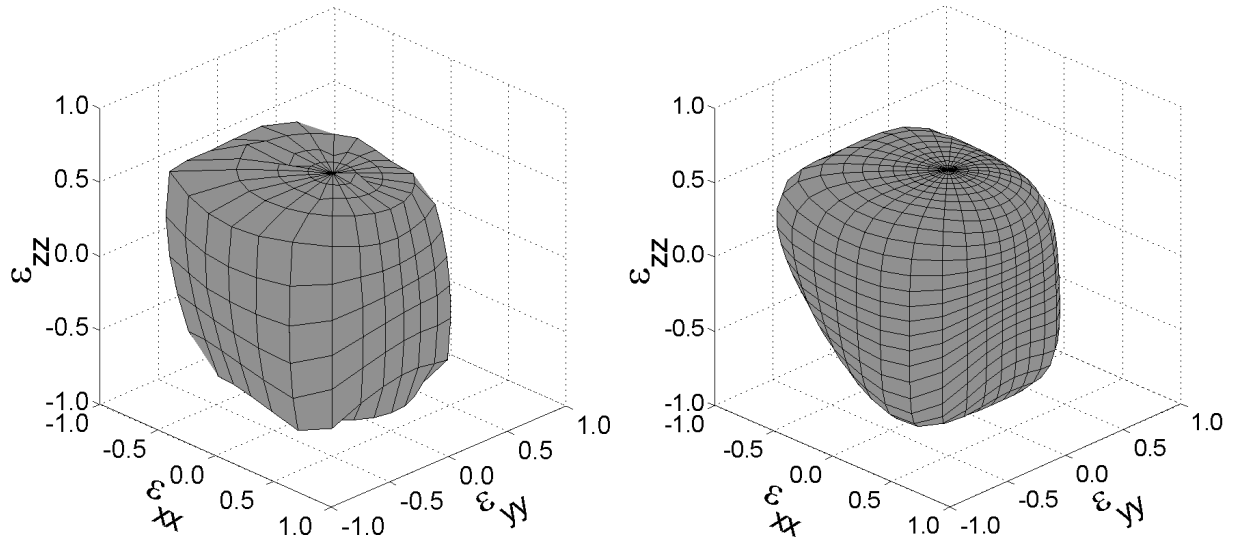
Figure 2

Figure 3
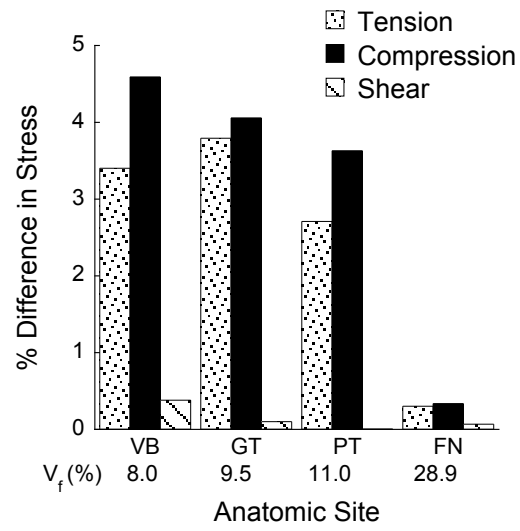
a)

b)

c)

Figure 4
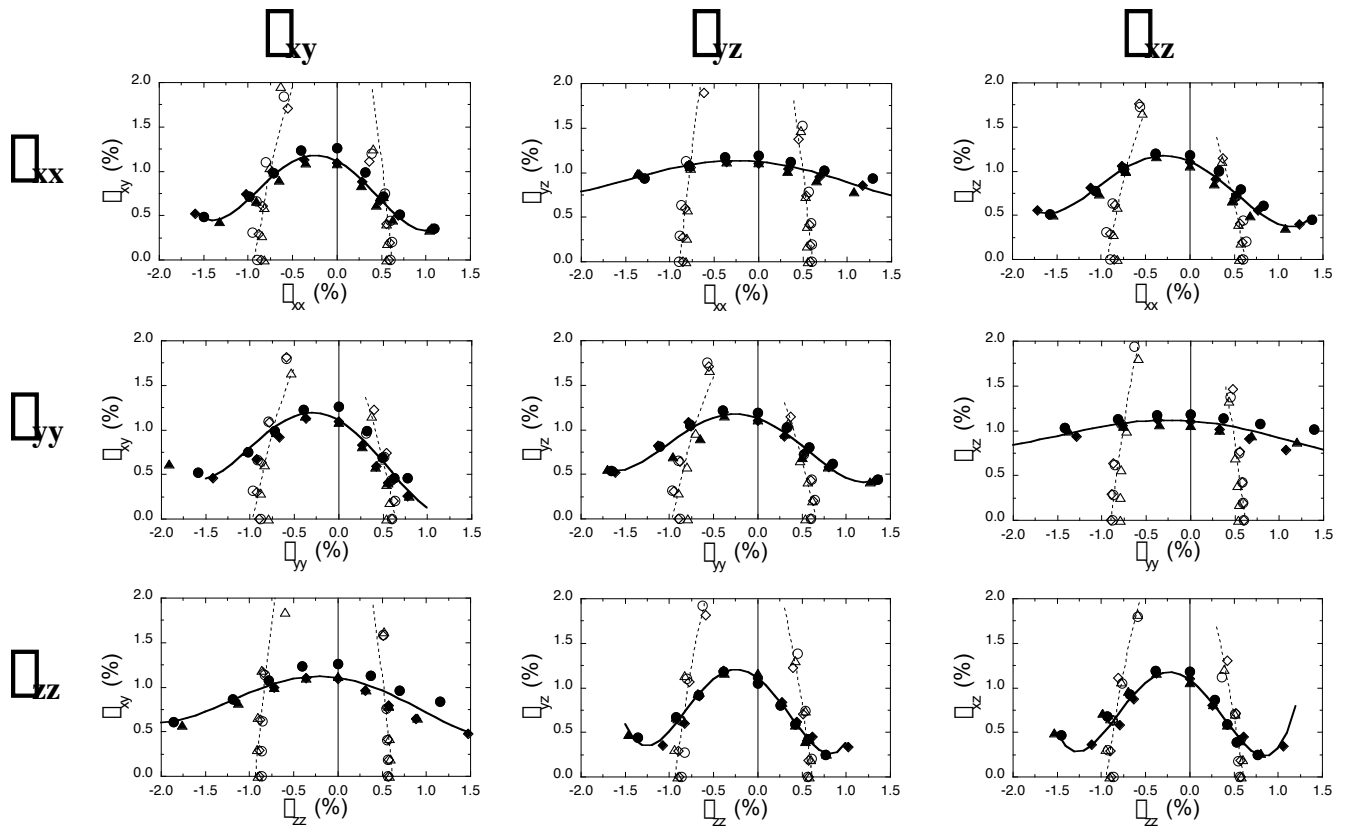
Figure 5

Figure 6

Figure 7

Figure 8